Engineering Dynamical Sweet Spots to Protect Qubits from 1/f Noise

Ziwen Huang,[1] Pranav S. Mundada,[2] Andrs Gyenis,[2] David I. Schuster,[3] Andrew A. Houck,[2] and Jens Koch[1]

[1]*Department of Physics and Astronomy, Northwestern University, Evanston, Illinois 60208, USA*
[2]*Department of Electrical Engineering, Princeton University, Princeton, New Jersey 08544, USA*
[3]*The James Franck Institute and Department of Physics, University of Chicago, Chicago, Illinois 60637, USA*

Protecting superconducting qubits from low-frequency noise is essential for advancing superconducting quantum computation. We here introduce a protocol for engineering dynamical sweet spots which reduce the susceptibility of a qubit to low-frequency noise. Based on the application of periodic drives, the location of the dynamical sweet spots can be obtained analytically in the framework of Floquet theory. In particular, for the example of fluxonium biased slightly away from half a flux quantum, we predict an enhancement of pure-dephasing by three orders of magnitude. Employing the Floquet eigenstates as the computational basis, we show that high-fidelity single-qubit gates can be implemented while maintaining dynamical sweet-spot operation. We further confirm that qubit readout can be performed by adiabatically mapping the Floquet states back to the static qubit states, and subsequently applying standard measurement techniques. Our work provides an intuitive tool to encode quantum information in robust, time-dependent states, and may be extended to alternative architectures for quantum information processing.

I. INTRODUCTION

Low-frequency noise has been a limiting factor for dephasing times of many solid-state based qubits [1–23]. Superconducting qubits especially suffer from 1/f charge and flux noise [1–17]. A conventional way to improve dephasing times is to operate the qubit at so-called sweet spots [5–8]. These sweet spots correspond to extrema of the qubit's transition frequency [5], see Fig. 1(a) for an example. Another established method for improving dephasing times is dynamical-decoupling (DD) [17, 24–28], which is well-known in the context of NMR echo sequences [29–31], and has been successfully applied to superconducting qubits [17, 25].

In this paper, we propose a qubit protection protocol based on *dynamical* sweet spots [32–34]. Inspired by static sweet-spot operation and dynamical decoupling, this protocol employs a periodic drive to mitigate the dephasing usually induced by $1/f$ noise. Utilizing Floquet theory, we show that dynamical sweet spots represent extrema in the qubit's quasienergy difference, and thus generalize the concept of static sweet spots [Fig. 1(b)]. Notably, dynamical sweet spots are generally not isolated points, but rather form extended sweet-spot manifolds in parameter space. The multi-dimensional nature of dynamical sweet spots provides additional freedom to tune qubit properties such as the transition frequency while maintaining dynamical protection. We show that dynamical sweet-spot operation can simultaneously yield both long depolarization (T_1) and pure-dephasing times (T_ϕ).

This protection scheme can also be interpreted as a continuous version of DD [35]. Here, the sequences of ultra-short pulses widely used in many DD experiments are replaced by a periodic drive on the qubit, which is much easier to realize experimentally. In addition to earlier explorations in this direction [36–38], we here provide a systematic framework for locating dynamical sweet-spot manifolds in the relevant parameter space. This framework is general enough to cover a variety of qubit systems, and can be adapted to different types of coupling to external drives, as well as noise environments. The theoretical approach we develop allows us not only to predict the improvement of pure-dephasing times, but also to assess how dynamical depolarization times are affected by the driving. We further show that the protection scheme is compatible with concurrent gate operations, thus making it suitable for both quantum information storage and processing.

The paper is structured as follows. Throughout this paper, we consider the superconducting fluxonium qubit [7, 8, 11, 12, 39] a platform for illustrating the dynamical-protection protocol. We begin in Section II, with a description of this qubit and discuss its static coherence times in the absence of external driving. In Section III, we employ Floquet theory to derive expressions for the dynamical coherence times of the driven qubit. We then evaluate these expressions numerically in Section IV, and discuss the nature of the observed dynamical sweet spots associated with increases in coherence times. We illustrate how to perform gate operations and readout on such a driven qubit (Floquet qubit) in Section V, and finally

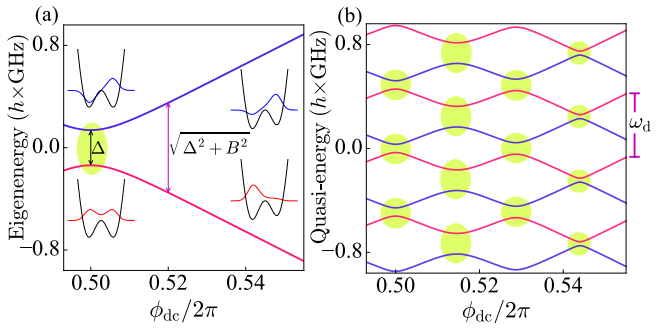

FIG. 1. (a) Static fluxonium spectrum as a function of magnetic flux. Insets show the qubit eigenfunctions at the sweet spot and slightly away from it ($\phi_\mathrm{dc}/2\pi = 0.52$). The parameters used are: $E_\mathrm{C}/h = 0.5\,\mathrm{GHz}$, $E_\mathrm{J}/h = 4.0\,\mathrm{GHz}$ and $E_\mathrm{L}/h = 1.3\,\mathrm{GHz}$ for the capacitive, Josephson and inductive energy, respectively. (b) Quasi-energy spectrum of the driven qubit for flux $\phi_\mathrm{ac}/2\pi = 0.028$ and drive frequency $\omega_\mathrm{d}/2\pi = 490\,\mathrm{MHz}$. The highlighted regions in both panels mark the flux sweet spots. The drive produces numerous dynamical sweet spots at different dc flux values, as opposed to only one in the static case.

present our conclusions in Section VI.

II. TWO-LEVEL SYSTEM SUBJECT TO 1/f NOISE

For concreteness, we discuss the application of the protection scheme to the fluxonium qubit [7, 8, 11, 12, 39], though the general theoretical framework is not limited to this choice. When the external flux bias in the circuit loop is tuned to the sweet spot at half a flux quantum, the fluxonium circuit exhibits long coherence times exceeding $100\,\mu$s and is strongly anharmonic [7, 8]. However, this sweet spot that is defined by the vanishing flux derivative of the qubit energy is point-like, and the qubit regains sensitivity to $1/f$ flux noise when the external flux is tuned slightly away from half a flux quantum [7, 8, 11, 12]. It is thus desirable to find versatile ways of protection from $1/f$ flux noise, and further improve coherence times.

Our protection scheme is based on introducing a modulation of the external flux close to the static sweet spot, i.e., $\phi_{\rm ext}(t) = \phi_{\rm ac}\cos(\omega_{\rm d}t) + \phi_{\rm dc}$. Here, $\phi_{\rm ext} = 2\pi\Phi_{\rm ext}/\Phi_0$ denotes the reduced external flux, Φ_0 is the flux quantum, and $\phi_{\rm ac}$, $\phi_{\rm dc}$ are its ac modulation amplitude and dc offset, respectively. Upon truncation to two levels, the effective Hamiltonian of the driven fluxonium circuit is given by

$$H_{\rm q}(t) = \frac{\Delta}{2}\hat{\sigma}_x + \left(A\cos\omega_{\rm d}t + \frac{B}{2}\right)\hat{\sigma}_z, \tag{1}$$

see Appendix A for details. Here, Δ denotes the qubit splitting at $\phi_{\rm dc} = \pi$, and $A \propto \phi_{\rm ac}$ and $B \propto \delta\phi_{\rm dc} = \phi_{\rm dc} - \pi$ are the effective drive amplitude and dc bias away from the static sweet spot. Note that we also set $\hbar = 1$ in this expression. The resulting eigenenergies of the static qubit ($\phi_{\rm ac} = 0$) are plotted in Fig. 1(a) as a function of $\phi_{\rm dc}$. The full Hamiltonian including the qubit-bath coupling is given by $H = H_{\rm q}(t) + H_{\rm B} + H_{\rm int}$, where $H_{\rm B}$ and $H_{\rm int}$ denote the Hamiltonian of the bath and the qubit-bath interaction. We consider two major noise sources that often limit fluxonium coherence times: $1/f$ flux noise and dielectric loss [7, 8, 12–15]. The corresponding interaction Hamiltonian thus takes the form $H_{\rm int} = (\hat{\eta}_{\rm f} + \hat{\eta}_{\rm d})\hat{\sigma}_z$, where $\hat{\eta}_{\rm f}$ and $\hat{\eta}_{\rm d}$ are the bath operators through which $1/f$ flux noise and dielectric loss are induced. The noise spectra characterizing these channels are given by $S_{\rm f}(\omega) = \mathcal{A}_{\rm f}^2|\omega/2\pi|^{-1}$ and $S_{\rm d}(\omega) = \alpha(\omega,T)\mathcal{A}_{\rm d}(\omega/2\pi)^2$ [40]. Here, $\alpha(\omega,T) = |\coth(\omega/2k_{\rm B}T) + 1|/2$ is a thermal factor, $k_{\rm B}$ and T denote the Boltzmann constant and temperature, and $\mathcal{A}_{\rm f}$ and $\mathcal{A}_{\rm d}$ denote the noise amplitudes.

As reference for our discussion of dynamical coherence times in Secs. III and IV, we first briefly review the static coherence times of the undriven qubit. The decoherence rates depend on the matrix elements of the qubit operator coupling to the noise as well as the noise spectra. For a non-singular noise spectrum $S(\omega)$, the rates for relaxation, excitation and pure dephasing are

$$\gamma_{\mp} = |\sigma_z^{ge}|^2\, S(\pm\Omega_{ge}), \tag{2}$$

$$\gamma_{\phi} = |\sigma_z^{ee} - \sigma_z^{gg}|^2\, S(0)/2. \tag{3}$$

Here, $|g\rangle$ and $|e\rangle$ denote the qubit ground and first excited state, $\Omega_{ge} = \sqrt{\Delta^2 + B^2}$ the corresponding eigenenergy difference, and $\sigma_z^{ll'} \equiv \langle l|\hat{\sigma}_z|l'\rangle$ $(l,l' = g,e)$ the relevant matrix elements. (Since these matrix elements will appear rather frequently, we choose to introduce this slightly more compact notation.) The quantity $|\sigma_z^{ee} - \sigma_z^{gg}|$ governing the pure-dephasing rate γ_ϕ turns out to be proportional to the flux dispersion of the eigenenergy difference $|\partial\Omega_{ge}/\partial\phi_{\rm dc}|$, in agreement with the well-known proportionality $\gamma_\phi \propto (\partial\Omega_{ge}/\partial\phi_{\rm dc})^2$ [5, 6]. For the realistic noise spectrum $S(\omega) = S_{\rm d}(\omega) + S_{\rm f}(\omega)$, however, there is a divergence at $\omega = 0$ from the $1/f$ flux noise. In this case, our evaluation of dephasing times includes careful consideration of frequency cutoffs, see Refs. [5, 6, 32, 41].

The resulting coherence times differ characteristically according to the flux bias. Away from the flux sweet spot, the qubit has wavefunctions with disjoint support [insets of Fig. 1(a)]. This leads to a suppression of the coefficient $|\sigma_z^{ge}|^2$ relevant for relaxation and excitation, and hence to a relatively long depolarization time of $T_1 = 770\,\mu$s (see Table I caption for our specific choice of parameters). The pure-dephasing time of $T_\phi = 0.88\,\mu$s is rather short, on the other hand, since the flux dispersion $\partial\Omega_{ge}/\partial\phi_{\rm dc}$ is significant away from the flux sweet spot. At the flux sweet spot, the situation changes: disjointness of eigenfunctions is lost and depolarization times are correspondingly shorter, $T_1 = 360\,\mu$s. Since the flux dispersion $\partial\Omega_{ge}/\partial\phi_{\rm dc}$ vanishes at the sweet spot, the qubit is less sensitive to $1/f$ noise, resulting in a pure-dephasing time exceeding 10 ms [7, 42], limited only by second-order contributions from $1/f$ flux noise. In realistic settings, the pure-dephasing times will be limited by other sources including photon shot noise, critical current noise, etc.

III. DYNAMICAL COHERENCE TIMES OF THE DRIVEN QUBIT

The analysis of coherence times must be modified when including a periodic drive acting on the qubit. Based on an open-system Floquet theory [43, 44], the coherence times are most conveniently characterized in the basis formed by the qubit's Floquet states. The quasi-energies ϵ_j and time-periodic Floquet states $|w_j(t)\rangle$ of the driven qubit, labeled by index j, are the counterparts of the ordinary eigenstates and eigenenergies in the undriven case [44–47]. They are obtained as solutions of the Floquet equation

$$\left[H_{\rm q}(t) - i\frac{\partial}{\partial t}\right]|w_j(t)\rangle = \epsilon_j|w_j(t)\rangle. \tag{4}$$

In the absence of noise, the evolution operator $U_{\rm q}(t,0) = \sum_{j=0,1}|w_j(t)\rangle\langle w_j(0)|\exp(-i\epsilon_j t)$ governs the evolution of the driven qubit. As a result, the population in each Floquet state remains invariant, while the relative phase accumulates at a rate given by the quasi-energy difference $\epsilon_{01} \equiv \epsilon_1 - \epsilon_0$.

The matrix elements and noise frequencies relevant for the decoherence of the driven qubit crucially differ from the undriven case. By casting the expression for the decoherence

rates into the form

$$\gamma_\mu = \int_{-\infty}^{\infty} F_\mu(\omega) S(\omega) \mathrm{d}\omega, \tag{5}$$

these differences are conveniently captured as a change in the filter function $F_\mu(\omega)$ [14, 48]. Here, $\mu = \mp, \phi$ denotes the different noise channels corresponding to relaxation, excitation and pure dephasing.

For the undriven qubit, $F_\mu(\omega)$ is strongly peaked at the filter frequencies $\omega = \pm\Omega_{ge}$ and $\omega = 0$. The integrated peak areas, referred to as weights, are given by the quantities $|\sigma_z^{ge}|^2$, $|\sigma_z^{eg}|^2$ and $|\sigma_z^{ee} - \sigma_z^{gg}|^2/2$ associated with the three noise channels. By contrast, for the driven qubit, $F_\mu(\omega) \sim \sum_k |g_{k,\mu}|^2 \delta(\omega - \bar{\omega}_{k,\mu})$ develops additional sideband peaks, resulting in filter frequencies $\bar{\omega}_{k,\mp} = \pm\epsilon_{01} - k\omega_\mathrm{d}$ and $\bar{\omega}_{k,\phi} = -k\omega_\mathrm{d}$ ($k \in \mathbb{Z}$). The corresponding weights are $|g_{k,\mp}|^2$ and $2|g_{k,\phi}|^2$, where

$$g_{k,+} = \frac{\omega_\mathrm{d}}{2\pi} \int_0^{2\pi/\omega_\mathrm{d}} dt\, e^{ik\omega_\mathrm{d} t}\, \mathrm{Tr}\left(\sigma_z |w_1(t)\rangle\langle w_0(t)|\right), \tag{6}$$

and similar expressions hold for $g_{k,-}$ and $g_{k,\phi}$ (see Appendix B). Expressed in terms of these weights, the decoherence rates are given by

$$\gamma_\mp = \sum_{k\in\mathbb{Z}} |g_{k,\mp}|^2 S(k\omega_\mathrm{d} \pm \epsilon_{01}), \tag{7}$$

$$\gamma_\phi = \mathcal{A}_f |2g_{0,\phi}| \sqrt{|\ln \omega_\mathrm{ir} t_\mathrm{m}|} + \sum_{k\neq 0} 2|g_{k,\phi}|^2 S(k\omega_\mathrm{d}), \tag{8}$$

where the infrared cutoff ω_ir and a finite measurement time t_m are introduced to regularize the singular behavior of the $1/f$ noise spectrum (see Appendix C). We note that Eqs. (7) and (8) are based on the rotating-wave approximation described in Appendix B. Further, it is instructive to mention that the expressions for the dynamical rates [Eqs. (7) and (8)] reduce to the rates obtained for the static case when the drive is switched off ($A = 0$). To see this, note that the Floquet states are time-independent for $A = 0$. As a result, the filter weights vanish for $k \neq 0$ [see, for example, Eq. (6)]. The remaining quantities to be identified are simply: $\pm\Omega_{ge} \leftrightarrow \bar{\omega}_{0,\mp}$, $0 \leftrightarrow \bar{\omega}_{0,\phi}$, and $|\sigma_z^{ge}|^2$, $|\sigma_z^{eg}|^2$, $|\sigma_z^{ee} - \sigma_z^{gg}|^2/2 \leftrightarrow |g_{0,\mp}|^2$ and $2|g_{0,\phi}|^2$.

IV. DYNAMICAL SWEET SPOTS

We numerically calculate the dynamical coherence times as a function of drive frequency and amplitude, for a flux bias fixed close to the half-integer point. Results of pure-dephasing times are presented in Fig. 2 (a), and show broad regions where $T_\phi = \gamma_\phi^{-1}$ remains close to the value of the undriven qubit, but also exhibit well-defined maxima where pure-dephasing times exceed 1 ms. (This value is based on the noise sources included in our analysis, but may ultimately be limited by other noise channels.) Fig. 2(b) shows the corresponding depolarization times $T_1 = (\gamma_+ + \gamma_-)^{-1}$. While there are point-like dropouts of T_1 for certain drive parameters, the majority of the predicted T_1's are well over $100\,\mu$s. Table I summarizes the coherence times for two example working points ① and ② aligned with local maxima of T_ϕ. The pure-dephasing times for both points exceed 1 ms, much longer than those of the undriven qubit. The depolarization times at those two points are around $500\,\mu$s, which are favorable compared to the static sweet-spot value.

TABLE I. Calculated coherence times for four operating points. Without a drive and operated away from the sweet spot ($\delta\phi_\mathrm{dc} = 0.02$), the qubit has the longest T_1 but the shortest T_ϕ. At the sweet spot, this behavior reverses: the static T_1 reaches maximum values, but T_ϕ becomes relatively short. By comparison, Floquet operation at dynamical sweet spots yields T_1 and T_ϕ values that do not exceed the static maximal values, but are well above the minimal ones. [Underlying parameter choices: The noise amplitudes used are $\mathcal{A}_\mathrm{d} = \pi^2 \tan\delta_\mathrm{C} |\tilde{\varphi}_{ge}|^2/E_\mathrm{C}$ and $\mathcal{A}_\mathrm{f} = 2\pi\delta_\mathrm{f} E_\mathrm{L} |\tilde{\varphi}_{ge}|$, where $\tilde{\varphi}_{ge} = \langle g|\hat{\varphi}|e\rangle$ is evaluated at $\phi_\mathrm{dc}/2\pi = 0.5$, and $\hat{\varphi}$ is the phase operator. We assume the loss tangent $\tan\delta_\mathrm{C} = 1.1 \times 10^{-6}$, flux-noise amplitude $\delta_\mathrm{f} = 1.8 \times 10^{-6}$, and a temperature of 15 mK.]

Working points	T_1 (μs)	T_ϕ (μs)
Away from the static sweet spot	**770**	0.88
Dynamical sweet spot ①	590	1200
Dynamical sweet spot ②	490	1750
Static sweet spot	360	**$>10^4$**

A. Asymptotic behavior of sweet manifolds for weak and strong drive

The regions where T_ϕ becomes maximal, form curves in the plane spanned by the drive frequency and amplitude, with distinct behavior in the two regimes of weak driving, $A \ll \Omega_{ge}$ [bottom of Fig. 2(a)], and strong driving, $A \gtrsim \Omega_{ge}$ [top of Fig. 2(a)]. These curves are the cross-sections of the sweet-spot manifolds at a fixed dc flux value $\delta\phi_\mathrm{dc}$, see Fig. 2(c). The curves of maximal pure-dephasing times show simple asymptotic behavior in these two limits, where they approach fixed-frequency intercepts in the A–ω_d plane. In the strong-drive limit, these curves are interrupted by cuts (see white arrows) where the width of the peak in $T_\phi(\omega_\mathrm{d})|_{A=\mathrm{const}}$ goes to zero. No such cuts are present in the weak-drive regime; rather, the peak width gradually decreases as drive amplitude A is lowered.

This behavior of pure-dephasing times of the driven qubit can be explained and approximated analytically using Floquet theory. Away from dynamical sweet manifolds, T_ϕ is limited by contributions from the (regularized) pole of the $1/f$ spectrum, see the first term on the right-hand side of Eq. (8). Thus, $\gamma_\phi \propto |g_{0,\phi}|$ which in turn can be shown to be proportional to $\partial\epsilon_{01}/\partial\phi_\mathrm{dc}$ (see derivation in Appendix D), i.e., the dynamical flux-noise sensitivity given by the flux dispersion of the Floquet quasi-energy difference. We emphasize that this result is analogous to the more familiar case of the undriven qubit, where the pure-dephasing rate is proportional to

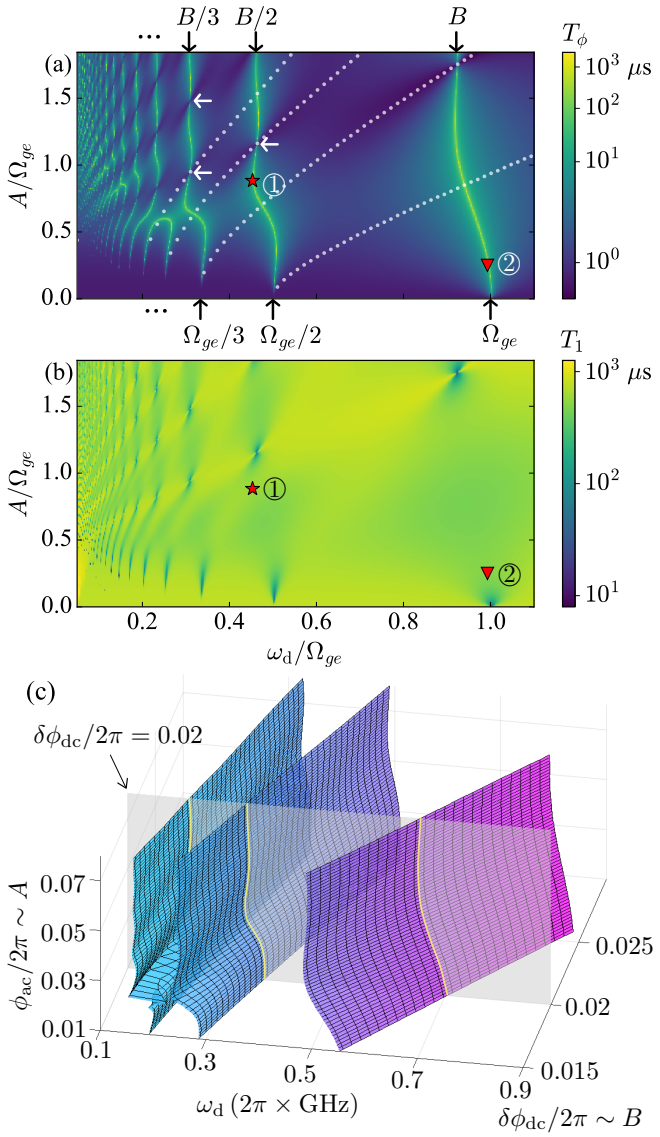

FIG. 2. (a) Dynamical pure-dephasing time T_ϕ (color-coded) as a function of drive frequency ω_d (horizontal axis) and drive amplitude A (vertical axis). Results are calculated via Eq. (8) for flux $\delta\phi_\mathrm{dc}/2\pi = 0.02$. The curves visible by their bright-yellow coloring are the dynamical sweet spots characterized by large T_ϕ. In the weak ($A \ll \Omega_{ge}$) and strong drive limit ($A \gtrsim \Omega_{ge}$) these curves asymptotically line up with $\omega_\mathrm{d} = \Omega_{ge}/m$ and $\omega_\mathrm{d} = B/m$ (black arrows). The curves formed by the dynamical sweet spots are interrupted by cuts marked by white arrows. The overlaid white dotted curves depict the ac dynamical sweet spots corresponding to $\partial\epsilon_{01}/\partial\phi_\mathrm{ac} = 0$. (b) Depolarization time T_1 calculated by Eq. (7). The majority of the obtained T_1 values are at the order of 500 μs, except for point-like dropouts shown by the dark-blue coloring. The red star and triangle specify the dynamical sweet spots ① and ②. The noise parameters used for the calculation are given in the caption of Table I. (c) Sweet-spot manifolds embedded in the 3d parameter space, with axes corresponding to ω_d, $\delta\phi_\mathrm{dc}$ and ϕ_ac. The semi-transparent plane given by $\delta\phi_\mathrm{dc}/2\pi = 0.02$, intersects the manifolds and thus yields the sweet-spot curves shown in (a) as cross sections (bright-yellow coloring).

the static flux dispersion $\partial\Omega_{ge}/\partial\phi_\mathrm{dc}$, with quasi-energies replaced by eigenenergies.

Pure-dephasing times are maximal whenever $\partial\epsilon_{01}/\partial\phi_\mathrm{dc}$ vanishes, which generically occurs at avoided crossings in the extended quasi-energy spectrum [Fig. 1(b)]. The latter, analogous to the extended Brillouin zone in spatially periodic systems, consists of the extended set of quasi-energies $\epsilon_{j,n} = \epsilon_j + n\omega_\mathrm{d}$ ($n \in \mathbb{Z}$) [44, 45]. This extended spectrum shows numerous avoided level crossings, and hence a multitude of regions of maximal T_ϕ. We refer to these operation points as *dynamical sweet spots*. As shown in Fig. 2(a), these spots form a set of curves with maximal T_ϕ in the A-ω_d plane. Once we account for the additional perpendicular axis representing B, we find that each curve is the cross-section of a continuous surface of sweet spots, which we refer to as a sweet-spot manifold. The locations of sweet spots can be predicted in the limits of weak and strong drive, by treating either the drive $A\cos\omega_\mathrm{d}t\,\sigma_z$ or the transverse qubit Hamiltonian $\Delta\,\sigma_x/2$ perturbatively.

Weak-drive limit.— For $A \ll \Omega_{ge}$, the unperturbed quasi-energies are the static eigenenergies up to the addition of integer multiples of the drive frequency, $\epsilon_{\pm,n} = \pm\Omega_{ge}/2 + n\omega_\mathrm{d}$ ($n \in \mathbb{Z}$). Two levels exhibit a crossing, $\epsilon_{+,n} = \epsilon_{-,n'}$, whenever the qubit frequency is an integer multiple of the drive frequency, $\Omega_{ge} = m\omega_\mathrm{d}$ where $m = n' - n \in \mathbb{N}$. The perturbation lifts these degeneracies and generates avoided crossings. As a result, the sweet spots observed towards the bottom of Fig. 2(a) asymptotically take the form of vertical lines at drive frequencies set by $\omega_\mathrm{d} = \Omega_{ge}/m$. The width of maxima in $T_\phi(\omega_\mathrm{d})$ is significant for the issue of parameter deviations: the wider the maximum, the larger is the robustness of the coherence-time increase with respect to small detunings from the dynamical sweet spot. This width is proportional to the gap size of the avoided crossing and given by $\Delta_m \approx A^m|\sin\theta\cos^{m-1}\theta|/\omega_\mathrm{d}^{m-1}(m-1)!$ in the weak-drive limit, where $\theta = \tan^{-1}(\Delta/B)$ (see derivation in Appendix D). For decreasing drive strength A, the width narrows with $\sim A^m$ consistent with the behavior observed in Fig. 2(a).

Strong-drive limit.— For $A \gtrsim \Omega_{ge}$, the unperturbed quasi-energies are given by $\epsilon_{\pm,n} = \pm B/2 + n\omega_\mathrm{d}$ ($n \in \mathbb{Z}$) and cross whenever $B = m\omega_\mathrm{d}$ ($m \in \mathbb{N}$) [45, 47, 49]. The perturbation $\Delta\sigma_x/2$ generically opens up gaps. The resulting sweet spots asymptotically line up with vertical intercepts $\omega_\mathrm{d} = B/m$, as shown in Fig. 2(a). The proportionality between the width of the maximal T_ϕ and the gap size also holds in this limit, with the latter given by $\Delta_m \approx \Delta|J_m(2A/\omega_\mathrm{d})|$ (see derivation in Appendix D). Whenever $\Delta_m = 0$, i.e., $2A/\omega_\mathrm{d}$ is one of the roots of the Bessel function J_m, the width goes to zero and the sweet-spot curve is interrupted with a cut.

The dropouts of T_1 visible in Fig. 2(b) are similarly related to the vanishing gap size of the avoided crossings. If the gap opening of the avoided crossing, i.e., the quasi-energy difference of the qubit at the dynamical sweet spot becomes smaller, the terms $|g_{0,\mp}|^2 S(\pm\epsilon_{01})$ in Eq. (7) rapidly increase in magnitude as the regularized divergence of $S(\omega)$ is sampled. In other words, the low-frequency $1/f$ noise significantly suppresses the dynamical T_1 whenever ϵ_{01} vanishes. Therefore, the low-T_1 features observed in Fig. 2(b) match the locations

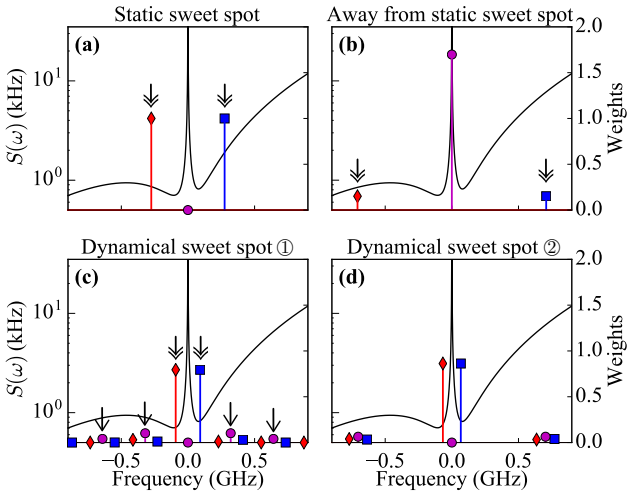

FIG. 3. Noise spectra and filter weights centered at the corresponding filter frequencies. The panels refer to four different working points: (a) the static sweet spot, (b) static operation away from the sweet spot ($\phi_{\rm dc}/2\pi = 0.52$), (c)-(d)dynamical sweet-spot operation at the working points ① and ②. The symbols represent relaxation (blue squares), excitation (red diamonds), and pure dephasing (purple dots). The noise spectrum is plotted concurrently in (a)-(d). The positions of filter frequencies and the associated filter weights determine which components of the noise spectrum contribute significantly to the rates $\gamma_\pm$ and γ_ϕ [see Eqs. (7) and (8)]. (See the main text for the discussion of filter frequencies marked by arrows.)

of strong narrowing of the maximal T_ϕ regions in Fig. 2(a) ($\Delta_m \to 0$), including the discussed cuts in the strong-drive limit, as well as the gradual narrowing in the weak-drive limit. In our example, the widths of T_ϕ peaks surrounding the sweet-spot manifolds are generally sufficiently wide and, hence, gap sizes sufficiently large, such that $1/f$ flux noise does not limit the dynamical T_1.

Driving the qubit, as discussed above, efficiently decouples it from the low-frequency dc flux noise. Recent experimental evidence points to the relevance of additional noise in the ac drive amplitude [32–34, 50]. While the magnitude and power spectrum of this noise are not well established, it is useful to note that there exist simultaneous sweet spots for the dc and ac flux amplitude, $\partial\epsilon_{01}/\partial\phi_{\rm dc} = \partial\epsilon_{01}/\partial\phi_{\rm ac} = 0$. These doubly-sweet spots correspond to intersection points of the white dotted curves ($\partial\epsilon_{01}/\partial\phi_{\rm ac} = 0$) and the underlying dc sweet-spot curves obtained for $\partial\epsilon_{01}/\partial\phi_{\rm dc} = 0$ [see Fig. 2(a)]. Depending on the magnitude of this ac noise, we expect such doubly-sweet spots to form the optimal working points.

B. Interpretation of coherence times in terms of filter functions

We observe that, although the obtained dynamical T_1 and T_ϕ times in the sweet manifolds do not exceed the maximal values at the two static working points (see Table I), they are well above the corresponding static minimal values. To understand this behavior, it is instructive to interpret the decoherence rates in terms of the sampling of the noise spectrum by the filter function [Eq. (5)]. For that purpose, Fig. 3 shows the noise spectrum $S(\omega)$ along with information characterizing the filter function $F_\mu(\omega)$ in terms of the relevant filter frequencies and weights. The noise spectrum (black curve) is peaked at $\omega = 0$ due to the $1/f$ flux noise; away from that peak, dielectric loss dominates. For each filter frequency, the value of the corresponding filter weight is shown and marked by symbols distinguishing between depolarization and pure-dephasing channels. While there are only three filter frequencies in the static case, the dynamical case in principle produces an infinite number of filter frequencies $\bar\omega_{k,\mu}$.

We first interpret the behavior of pure-dephasing times. The weight related to filter frequency $\bar\omega_{0,\phi}$ is suppressed to zero for both static and dynamical sweet spots [see Fig. 3(a),(c),(d)], but is large for the working point away from sweet spot [see Fig. 2(b)]. This weight reflects the qubit's sensitivity to $1/f$ flux noise. Therefore, the T_ϕ times at the sweet spots (both static and dynamical) are significantly longer than the one at the non-sweet spot. Compared with T_ϕ at the static sweet spot, the dynamical sweet spots exhibit somewhat lower values of T_ϕ. This is related to the small but nonzero pure-dephasing weights at filter frequencies $\bar\omega_{k,\phi} \neq 0$, absent for static sweet spots. Figure 3(c) illustrates this for the working point ①, where the relevant weights resulting in the dynamical $T_\phi \approx 1\,$ms are marked by single-headed arrows. (The same reasoning applies to the other working point ②.)

The behavior of depolarization times T_1 at and away from sweet spots is reversed relative to that of T_ϕ. Specifically, T_1 is longest at the static *non-sweet spot*, where disjoint support of wave functions leads to the strongly suppressed weights marked by double-headed arrows in Fig. 3(b). By contrast, depolarization weights for *sweet spots* [both static and dynamical, Figs. 3(a),(c)] are not subject to this suppression and produce correspondingly lower T_1. [The T_1 trend obtained from the analysis of weight suppression is partially offset by the fact that $S(\omega)$ is filtered at different frequencies in the sweet-spot vs. non-sweet-spot case.] Next, the comparison shows that the static depolarization time at the sweet spot is smaller than the dynamical T_1. The reason for this can be traced to the difference in filter frequencies and corresponding magnitudes of the noise power spectrum, see Fig. 3(a) vs. (c). In the static case, the filter frequencies for depolarization are $\pm\Omega_{ge}$, and $S(\pm\Omega_{ge})$ is relatively large compared to the dynamical case in 3(c) where the dominant contributions arise from $S(\bar\omega_{0,\pm})$. Indeed, these latter contributions closely match the minima of the noise power spectrum – a situation which can be established simply by tuning the drive parameters.

Inspection of Tab. I reveals a trend of T_1 and T_ϕ being anti-correlated: larger T_1 tend to coincide with with smaller T_ϕ and vice versa. This trend originates from the conservation of the cumulative filter weight,

$$(W_+ + W_-) + W_\phi = 2, \tag{9}$$

where $W_\pm = \sum_k |g_{k,\pm}|^2$ governs depolarization and $W_\phi = \sum_k 2|g_{k,\phi}|^2$ pure dephasing. (A proof of this conservation law is given in Appendix C.) Increases in depolarization weights thus go along with decreases in the pure-dephasing

weight, creating a tendency for trade-off between depolarization and dephasing which is exact only in the special case of white noise. This conservation rule is analogous to the sum rule that emerges in the context of dynamical decoupling [17, 26]. It is crucial that the conservation rule applies to filter weights rather than the rates. This enables one to manipulate the distribution of weights and filter frequencies to our advantage, putting the largest weights at or near minima in the noise spectrum.

V. QUBIT GATES AND READOUT

The above results suggest that use of the driven Floquet states as computational qubit states can be advantageous due to the long coherence times reached at the dynamical sweet spots. We refer to this dynamically protected qubit as the *Floquet qubit*. In the following, we show that such Floquet qubits are not only well-suited for quantum information storage, but can easily be integrated into gate and readout protocols necessary for quantum-information processing.

A. Gate operations

We show that we can realize direct single-qubit gates on the Floquet qubit. For example, X and $\sqrt{X}$ gates can be realized by inducing Rabi oscillations among Floquet eigenstates. This is accomplished by applying an additional pulse with carrier frequency $\omega'_{\rm d} \approx \epsilon_{01}$, duration $\tau_{\rm Rabi}$, and maximal amplitude $d_{\rm Rabi}$, see inset of Fig. 4(a). We verify the presence of Rabi oscillations numerically by simulating the time evolution for the working point ①. For a fixed initial state $|w_0(t)\rangle$, the final population of $|w_1(t)\rangle$ shows oscillatory behavior as a function of $\tau_{\rm Rabi}$ and $\omega'_{\rm d}$, see Fig. 4(a). Full Rabi cycles only occur when $\omega'_{\rm d}$ matches ϵ_{01}. Computation of the gate fidelities for the examples of X and $\sqrt{X}$ gates yields a value of 99.99% in both cases.

Single-qubit phase gates can be implemented by modulating the quasi-energy difference ϵ_{01} through a temporary increase δA of the drive amplitude [see inset of Fig. 4(b)]. This modifies the dynamical phase acquired over the gate duration $\tau_{\rm phase}$, enabling S and T gates, for example. For numerical verification, we initialize the qubit in one of the Floquet superposition states $|\psi_\pm(t)\rangle = [|w_0(t)\rangle \pm |w_1(t)\rangle e^{-i\epsilon_{01}t}]/\sqrt{2}$ (equator of the Bloch sphere) and monitor the population in the orthogonal state as a function of $\tau_{\rm phase}$ and δA. The observed oscillations [Fig. 4(b)] in this population indicates that the computational states accumulate a relative phase as expected. The computed fidelity for S $(\pi/2)$ and T $(\pi/4)$ gates realized both exceed 99.99%.

B. Readout

Floquet states can be adiabatically mapped [51] to the eigenstates of the driven qubit by slowly ramping down the flux modulation, provided that gaps in the quasi-energy spectrum are sufficiently large. For ①, Fig. 4(c) shows that quasi-energy gaps do not close as A is decreased to 0, thus enabling the adiabatic state transfer. We verify this mapping numerically by simulating the closed-system evolution with either

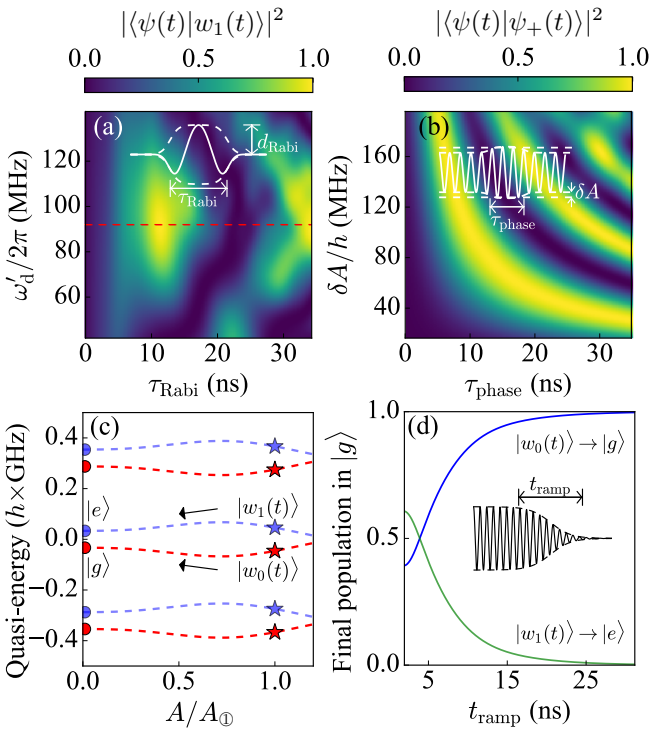

FIG. 4. Concurrent gates for the Floquet qubit and adiabatic mapping protocol for readout. (a) Adding a secondary pulse (inset) to the Floquet drive induces Rabi oscillations, which are sufficient for implementing X gate operations. The plot shows the final population in Floquet eigenstate $|w_1(t)\rangle$ as a function of pulse duration $\tau_{\rm Rabi}$ and carrier frequency $\omega'_{\rm d}$, for the initial state $|w_0(t)\rangle$. Full Rabi oscillations are observed when the secondary drive frequency matches the quasi-energy difference ϵ_{01} (dashed line) (b) Phase gates can be realized by a temporary increase in the Floquet drive strength (inset). The change in drive strength modulates the quasi-energy and thus enables phase gates such as $S\,(\pi/2)$ and $T\,(\pi/4)$. The plot shows the final population in $|\psi_+(t)\rangle$, as a function of the pulse duration $\tau_{\rm phase}$ and the drive amplitude variation δA, with the qubit initialized in $|\psi_-(t)\rangle$ (see main text for definition for $|\psi_\pm(t)\rangle$). (c) shows the quasi-energy spectrum as a function of A (from 0 to $A_①$), with Floquet drive frequency fixed at $\omega_{\rm d①}$. ($A_①$ and $\omega_{\rm d①}$ are the drive parameters at working point ①.) Red and blue star symbols mark the two Floquet states at point ①, whereas dots of the same color represent the states $|g\rangle$ and $|e\rangle$ of the undriven fluxonium. An adiabatic mapping from Floquet states to static qubit eigenstates can by realized with a sufficiently slow switch-off of the drive from $A_①$ to 0, given the nonzero gap between the quasi-energies. (d) Simulation of the adiabatic mapping achieved by continuously switching off the drive (ramp-down in inset). The final population in $|g\rangle$ is plotted as a function of the ramp time $t_{\rm ramp}$, with the qubit initiated in $|w_0(t)\rangle$ (blue) or $|w_1(t)\rangle$ (green). The results confirm the feasibility of an adiabatic mapping with high fidelity, thus enabling readout of the Floquet states.

of the driven Floquet qubit eigenstates $|w_{0(1)}(t)\rangle$ as the initial state and a smooth ramp-down of duration $t_{\rm ramp}$. Fig. 4(d) shows the calculated population in the undriven qubit eigenstates $|g(e)\rangle$ as a function of time. The resulting state-transfer fidelity is high for ramp times of the order of tens of ns, (99.6% for $t_{\rm ramp} = 30\,$ns). Conventional dispersive readout techniques, applicable to fluxonium qubits [7, 11–13], can then be employed subsequently in order to infer the original dynamical state.

VI. CONCLUSIONS

Operation of superconducting qubits at static sweet spots is a well-established means to reducing $1/f$ noise sensitivity. However, one limitation is the abrupt symmetry-induced change in the nature of wavefunctions at the sweet spot, which can negatively impact depolarization times at the sweet spot. We have presented a protocol for engineering dynamical sweet spots which partially overcome this limitation. In contrast to static sweet-spot operation, the Floquet scheme can yield long dynamical T_ϕ and T_1 simultaneously. The possibility to directly perform gate operations and readout on Floquet qubits makes them promising for both quantum information storage and processing. Future work will demonstrate how to realize multi-qubit gates on Floquet qubits while maintaining the dynamical sweet-spot protection.

ACKNOWLEDGMENTS

The work was supported by the Army Research Office under Grant No. W911NF-19-1-0016. We thank Xinyuan You, Daniel Weiss and Brian Baker for helpful discussion.

Appendix A: Effective model for fluxonium, and coupling to noise sources

The Hamiltonian describing a flux-modulated fluxonium is given by [52]

$$H_{\rm q,full}(t) = 4E_{\rm C}\hat{n}^2 + \frac{1}{2}E_{\rm L}[\hat{\varphi} + \phi_{\rm ext}(t)]^2 - E_{\rm J}\cos\hat{\varphi}, \tag{A1}$$

where $E_{\rm C}$, $E_{\rm L}$ and $E_{\rm J}$ represent the capacitive, inductive and Josephson energies of the fluxonium qubit, and $\phi_{\rm ext}(t) = \phi_{\rm dc} + \phi_{\rm ac}\cos(\omega_{\rm d}t)$. We use $\hat{\varphi}$ and $\hat{n}$ to denote the flux and conjugate charge operator of the qubit, respectively.

The static eigenenergies Ω_l and corresponding eigenstates $|l\rangle$ ($l = g, e, f, \cdots$) are obtained by diagonalizing $H_{\rm q,full}$, and depend on the dc flux component $\phi_{\rm dc}$. We will refer to the specific solutions at the static sweet spot $\phi_{\rm dc} = \pi$ by $\widetilde{\Omega}_l$ and $|\tilde{l}\rangle$. These eigenstates, expressed in the phase basis, have alternating parities (for example, $|\tilde{g}\rangle$ and $|\tilde{e}\rangle$ have even and odd parities respectively).

To avoid leakage into higher fluxonium states under flux modulation, we choose fluxonium parameters resulting in a large anharmonicity at half-integer flux, $\widetilde{\Omega}_f - \widetilde{\Omega}_e \gg \widetilde{\Omega}_e - \widetilde{\Omega}_g$. If we limit the external flux $\phi_{\rm ext}(t)$ to values in the vicinity of $\phi_{\rm dc} = \pi$, and avoid resonance with the $e-f$ transition, $\omega_{\rm d} \ll \widetilde{\Omega}_f - \widetilde{\Omega}_e$, then Eq. (A1) can be approximated by the effective two-level Hamiltonian (1). In that Hamiltonian, $\Delta = \widetilde{\Omega}_e - \widetilde{\Omega}_g$, $A = E_{\rm L}\phi_{\rm ac}\tilde{\varphi}_{ge}$, $B = 2E_{\rm L}(\phi_{\rm dc} - \pi)\tilde{\varphi}_{ge}$; here, $\tilde{\varphi}_{ge} = |\langle\tilde{g}|\hat{\varphi}|\tilde{e}\rangle|$. Different from the usual convention, we define the Pauli matrices as

$$\sigma_x = |\tilde{e}\rangle\langle\tilde{e}| - |\tilde{g}\rangle\langle\tilde{g}|, \quad \sigma_z = |\tilde{g}\rangle\langle\tilde{e}| + |\tilde{e}\rangle\langle\tilde{g}|, \tag{A2}$$

which is a common choice in the context of flux qubits [45, 46].

Given this effective model, it is important to revisit the question of how the fluxonium qubit couples to the limiting environment degrees of freedom. In Section II, it is posited that the noise sources of interest couple to the qubit through its σ_z operator which can be motivated as follows. The fluxonium's interaction with the $1/f$ flux noise source can be modeled as mutual inductance between the fluxonium's inductor and the bath, hence the coupling to the noise is via the qubit operator $\hat{\varphi}$. Experimental results are further consistent with dielectric noise coupling to the qubit's phase operator [7, 8, 12, 13, 15]. Note that operator $\hat{\varphi}$ only couples states with different parities. Therefore, based on Eq. (A2), it is projected to σ_z in the two-level subspace, which results in the $H_{\rm int}$ used in our model.

Appendix B: Floquet master equation

This appendix sketches the derivation of the Floquet master equation [43, 44, 47] which we use in the subsequent appendix to calculate the dynamical decoherence rates. The full Hamiltonian is given by $H(t) = H_{\rm q}(t) + H_{\rm B} + H_{\rm int}$ with time-periodic qubit Hamiltonian, and time-independent bath and interaction Hamiltonian. The latter is taken to be of the form $H_{\rm int} = \hat{\sigma}\hat{\eta}$, where $\hat{\sigma}$ and $\hat{\eta}$ are qubit and bath operators, respectively.

We start from the Redfield equation of the driven qubit

$$\frac{{\rm d}\tilde{\rho}_{\rm q}(t)}{{\rm d}t} = -\int_0^t d\tau {\rm Tr}_{\rm B}\Big[\tilde{H}_{\rm int}(t), \Big[\tilde{H}_{\rm int}(t-\tau), \tilde{\rho}_{\rm q}(t)\otimes\tilde{\rho}_{\rm B}\Big]\Big], \tag{B1}$$

which describes the evolution of the qubit density matrix $\tilde{\rho}_{\rm q}$ (in the interaction picture). Here, ${\rm Tr}_{\rm B}$ denotes a partial trace on the bath degrees of freedom, and $\tilde{\rho}_{\rm B}$ is the density matrix of the bath in the interaction picture, which is assumed to stay in thermal equilibrium. The term $\tilde{H}_{\rm int}(t) = U_0^\dagger(t)H_{\rm int}U_0(t)$ is the qubit-bath coupling expressed in the interaction picture, where $U_0(t) = U_{\rm q}(t)U_{\rm B}(t)$, $U_{\rm q}(t) = \sum_{j=0,1}|w_j(t)\rangle\langle w_j(0)|\exp(-i\epsilon_j t)$, and $U_{\rm B}(t) = \exp(-iH_{\rm B}t)$. The interaction term can be further expressed as $\tilde{H}_{\rm int}(t) = \tilde{\sigma}(t)\tilde{\eta}(t)$, where $\tilde{\sigma}(t) = U_{\rm q}^\dagger(t)\hat{\sigma}U_{\rm q}(t)$ and $\tilde{\eta}(t) = U_{\rm B}^\dagger(t)\hat{\eta}U_{\rm B}(t)$.

Eq. (B1) is an integro-differential equation, and not convenient for reading off decoherence rates. To derive expressions for γ_μ ($\mu = \pm, \phi$), we first simplify this equation by

employing the rotating-wave approximation. In order to identify the fast-rotating terms, we decompose $\tilde{\sigma}(t)$ into different frequency components,

$$\tilde{\sigma}(t) = \sum_{k\in\mathbb{Z},\mu=\pm,\phi} g_{k,\mu}\hat{c}_\mu(0)\exp(i\bar{\omega}_{k,\mu}t). \tag{B2}$$

Here, we define the Floquet counterparts of the Pauli matrices by

$$\begin{aligned}\hat{c}_+(t) &= |w_1(t)\rangle\langle w_0(t)|,\\ \hat{c}_-(t) &= |w_0(t)\rangle\langle w_1(t)|,\\ \hat{c}_\phi(t) &= |w_1(t)\rangle\langle w_1(t)| - |w_0(t)\rangle\langle w_0(t)|.\end{aligned} \tag{B3}$$

The frequencies $\bar{\omega}_{k,\mu}$ appearing in Eq. (B2) are the filter frequencies defined in the Section III, namely $\bar{\omega}_{k,\pm} = \mp\epsilon_{01} - k\omega_\mathrm{d}$ and $\bar{\omega}_{k,\phi} = -k\omega_\mathrm{d}$. Furthermore, the Fourier-transformed coupling matrix elements are given by

$$\begin{aligned}g_{k,\pm} &= \frac{\omega_\mathrm{d}}{2\pi}\int_0^{2\pi/\omega_\mathrm{d}} \mathrm{d}t\, e^{ik\omega_\mathrm{d}t}\ \mathrm{Tr}_\mathrm{q}\left[\hat{\sigma}\hat{c}_\pm(t)\right],\\ g_{k,\phi} &= \frac{\omega_\mathrm{d}}{4\pi}\int_0^{2\pi/\omega_\mathrm{d}} \mathrm{d}t\, e^{ik\omega_\mathrm{d}t}\ \mathrm{Tr}_\mathrm{q}\left[\hat{\sigma}\hat{c}_\phi(t)\right],\end{aligned} \tag{B4}$$

where Tr_q is the partial trace over the qubit degrees of freedom.

The qubit interaction operator $\tilde{\sigma}(t)$, expanded in this way, is substituted into Eq. (B1) resulting in a sum terms each involving the coefficient $\exp[i(\bar{\omega}_{k',\mu'} - \bar{\omega}_{k,\mu})t]$. Under certain conditions, every term with $\bar{\omega}_{k',\mu'} - \bar{\omega}_{k,\mu} \neq 0$ can be treated as fast-rotating and be neglected. This strategy is appropriate if both the minimal quasi-energy difference and the drive frequency ω_d are much larger than the inverse of the relevant time scale, i.e., the coherence time. With this Eq. (B1) is cast into the simplified form

$$\frac{\mathrm{d}\tilde{\rho}_\mathrm{q}(t)}{\mathrm{d}t} = \sum_{\mu=\pm,\phi}\zeta_\mu\left[\int_{-\infty}^{\infty}\mathrm{d}\omega F_\mu(\omega,t)S(\omega)\right]\mathbb{D}[\hat{c}_\mu]\tilde{\rho}_\mathrm{q}(t), \tag{B5}$$

where

$$F_\mu(\omega,t) = \zeta_\mu^{-1}\sum_k \pi^{-1}t\,\mathrm{sinc}[(\omega-\bar{\omega}_{k,\mu})t]|g_{k,\mu}|^2 \tag{B6}$$

denotes the filter functions from Section III, $\mathbb{D}[L]\tilde{\rho}_\mathrm{q} = L\tilde{\rho}_\mathrm{q}L^\dagger - (L^\dagger L\tilde{\rho}_\mathrm{q} + \tilde{\rho}_\mathrm{q}L^\dagger L)/2$ is the usual damping superoperator, and $S(\omega) = \int_{-\infty}^{\infty}\mathrm{d}t\, e^{i\omega t}\,\mathrm{Tr}_\mathrm{B}[\tilde{\eta}(t)\tilde{\eta}(0)\tilde{\rho}_\mathrm{B}]$ is the noise spectrum. We have further introduced the abbreviations $\zeta_\pm \equiv 1$ and $\zeta_\phi \equiv 1/2$, and used $\hat{c}_\mu(0) \to \hat{c}_\mu$. [We note that terms contributing to the Lamb shift have been omitted in Eq. (B5).]

The simplified Redfield equation (B5) is reminiscent of the Lindblad form, and includes three distinct terms $\mu = \pm$ and $\mu = \phi$ that describe relaxation, excitation and pure dephasing of the Floquet qubit. However, in place of fixed rates associated with the individual jump terms, Eq. (B5) still involves time-dependent rate coefficients given by

$$K_\mu(t) = \int_{-\infty}^{\infty}\mathrm{d}\omega F_\mu(\omega,t)S(\omega). \tag{B7}$$

We discuss in the subsequent appendix how to evaluate these rate coefficients for concrete choices of the noise spectrum $S(\omega)$.

Appendix C: Evaluation of decoherence rates

This appendix discusses the evaluation of the decoherence rate coefficients associated with the simplified Redfield equation (B5), focusing on the specific noise spectrum $S(\omega)$ adopted in the main text. To simplify the integral $K_\mu(t)$, we first inspect the structure of the filter functions $F_\mu(\omega,t)$ defined in Eq. (B6). These functions are peaked at the filter frequencies $\bar{\omega}_{k,\mu}$, with the peak width given by $2\pi t^{-1}$. We distinguish two separate scenarios: (1) the case of noise spectra that can be approximated as constant within each peak width, and (2) the case of noise spectra, such as $1/f$ spectra, where this approximation does not hold for all peaks.

Case (1).—If the spectrum $S(\omega)$ is sufficiently flat within each peak-width frequency range, we can approximate $(t/\pi)\,\mathrm{sinc}(\omega t) \approx \delta(\omega)$ in Eq. (B6), and arrive at the Markovian Floquet master equation

$$\frac{\mathrm{d}\tilde{\rho}_\mathrm{q}(t)}{\mathrm{d}t} = \sum_{k\in\mathbb{Z},\mu=\pm,\phi}|g_{k,\mu}|^2 S(\bar{\omega}_{k,\mu})\mathbb{D}[\hat{c}_\mu]\tilde{\rho}_\mathrm{q}(t). \tag{C1}$$

This form allows one to directly read off the resulting rates which are given by $\gamma_\pm = \sum_k |g_{k,\mu}|^2 S(\bar{\omega}_{k,\pm})$ and $\gamma_\phi = \sum_k 2|g_{k,\phi}|^2 S(\bar{\omega}_{k,\phi})$.

Case (2).—On the other hand, the noise spectrum $S(\omega)$ at depolarization filter frequencies $\bar{\omega}_{k,\pm}$ is considered flat, therefore the resulting expressions of $\gamma_\pm$ is the same as shown in Case (1). Finally, we arrive at the results shown in Eqs. (7) and (8) in the main text.

Whenever the noise spectrum varies significantly across one filter-function peak width, the above approximation fails. This is, in particular, the case for $1/f$ noise near $\omega = 0$ where $S(\omega)$ is purely dominated by the contribution $S_\mathrm{f}(\omega) = \mathcal{A}_f^2|\omega/2\pi|^{-1}$. For filter frequencies away from $\omega = 0$, we continue treating $S(\omega)$ as sufficiently flat. Zero and nonzero filter frequencies hence play distinct roles. For depolarization, relevant filter frequencies $\bar{\omega}_{k,\pm}$ are non-zero and the discussion of Case (1) carries over, yielding Eq. (7) for the depolarization rates.

The appearance of a zero filter frequency for dephasing motivates us to separate the integral $K_\phi(t)$ [Eq. (B7)] into a low-frequency and a high-frequency part. We focus on the low-frequency part first, which is given by

$$I(t) = 2|g_{0,\phi}|^2\int_{-\pi/t}^{\pi/t}\mathrm{d}\omega\,\frac{t}{\pi}\,\mathrm{sinc}(\omega t)S_\mathrm{f}(\omega), \tag{C2}$$

where the integration range is set by the peak width $2\pi/t$. To regularize the logarithmic divergence of this integral, we employ infrared cutoffs $\pm\omega_\mathrm{ir}$ [5, 16, 32, 41]. The cutoff is of the order of 1 Hz [16], much smaller than the inverse of the measurement time. In this case, the integral can be approximated

by

$$I(t) \approx 8\mathcal{A}_{\rm f}^2 t|\ln\omega_{\rm ir}t||g_{0,\phi}|^2. \tag{C3}$$

For the integral over the remaining high-frequency range, the δ-function approximation we made in Case (1) is again valid. After combining the low and high-frequency contributions, the approximated $K_\phi(t)$ is a time-dependent function, given by

$$K_\phi(t) \approx I(t) + 2\sum_{k\neq 0}|g_{k,\phi}|^2 S(\bar{\omega}_{k,\phi}). \tag{C4}$$

According to this, $K_\phi(t)$ is reminiscent of a time-dependent rate for pure dephasing that grows linearly in time (up to logarithmic corrections). Consequently, the off-diagonal elements of the density matrix do not follow an exponential decay. Instead, the decay is given by

$$\tilde{\rho}_{\rm q,01} \sim \exp\Big[-4\mathcal{A}_{\rm f}^2|g_{0,\phi}|^2 t^2|\ln\omega_{\rm ir}t| - \sum_{k\neq 0}2|g_{k,\phi}|^2 S(\bar{\omega}_{k,\phi})t\Big], \tag{C5}$$

which is a product of a Gaussian (again, up to logrithmic corrections) and pure exponential. (Note that to estimate the pure-dephasing rate, the contribution of depolarization to the decay of $\tilde{\rho}_{\rm q,01}$ is excluded in the expression above.) Based on the $1/e$ decay time, we obtain

$$\gamma_\phi \simeq \mathcal{A}_{\rm f}|2g_{0,\phi}|\sqrt{|\ln\omega_{\rm ir}t_{\rm m}|} + \sum_{k\neq 0}2|g_{k,\phi}|^2 S(\bar{\omega}_{k,\phi}), \tag{C6}$$

as a simple approximation bounding the pure-dephasing rate from above. Here, $t_{\rm m}$ is the characteristic measurement time; a representative value of the factor $\sqrt{|\ln\omega_{\rm ir}t_{\rm m}|}$ found in a recent experiment [16] is close to 4.

As discussed in Section IV.B, there exists an interrelation constraining the depolarization and pure-dephasing rates. This constraint originates from the conservation rule (9) for the filter weights which we prove in the following. Without loss of generality, we take the qubit coupling operator $\hat{\sigma}$ in $H_{\rm int} = \hat{\sigma}\hat{\eta}$ to be traceless with eigenvalues ± 1. (Any trace contribution renormalizes the bath Hamiltonian, and the scale factor rendering the eigenvalues ± 1 can be absorbed into $\hat{\eta}$.) Employing the decomposition of the identity in terms of the Floquet states, $\mathbb{1} = \sum_{j=0,1}|w_j(t)\rangle\langle w_j(t)|$, and making use of Eqs. (B3) and (B4), we find

$$\begin{aligned}\mathrm{Tr}_{\rm q}(\hat{\sigma}^2) &= \mathrm{Tr}_{\rm q}(\hat{\sigma}\mathbb{1}\hat{\sigma}\mathbb{1}) = \sum_{j,j'=0,1}|\langle w_j(t)|\hat{\sigma}|w_{j'}(t)\rangle|^2 \\ &= \frac{1}{2}\big|\,\mathrm{Tr}_{\rm q}[\hat{\sigma}\hat{c}_z(t)]\big|^2 + \sum_{\mu=\pm}\big|\,\mathrm{Tr}_{\rm q}[\hat{\sigma}\hat{c}_\pm(t)]\big|^2 \\ &= \sum_{\mu=\pm,\phi}\zeta_\mu^{-1}\left|\sum_{k\in\mathbb{Z}} g_{k,\mu}\, e^{-ik\omega_{\rm d}t}\right|^2 = 2.\end{aligned} \tag{C7}$$

Time averaging this expression over one drive period $2\pi/\omega_{\rm d}$ finally yields the claimed conservation rule

$$W_+ + W_- + W_\phi = \sum_{k\in\mathbb{Z}}\left(|g_{k,+}|^2 + |g_{k,-}|^2 + 2|g_{k,\phi}|^2\right) = 2. \tag{C8}$$

We further note that Eq. (C8) also imposes a constraint on the filter functions, namely

$$\sum_{\mu=\pm,\phi}\int_{-\infty}^{\infty}\mathrm{d}\omega F_\mu(\omega,t) = 2. \tag{C9}$$

Appendix D: Analytical approach for solving Floquet equations

In this appendix, we first introduce a framework useful for solving the Floquet equation, and later employ this framework to derive several results discussed in Sections III and IV.

Solutions $|w_j(t)\rangle$ of the Floquet equation (4) are required to be time-periodic in $2\pi/\omega_{\rm d}$. Each such wavefunction can be considered an element in the vector space $\mathcal{F}$ of $2\pi/\omega_{\rm d}$-periodic functions of the type $f:\mathbb{R}\to\mathbb{C}^2$. We choose the basis vectors of $\mathcal{F}$ to be $|f_{\sigma,k}(t)\rangle = |\sigma\rangle\exp(-ik\omega_{\rm d}t)$, where $|\sigma = z^\pm\rangle$ are the eigenvectors of the operator $\hat{\sigma}_z$ and $k\in\mathbb{Z}$. In this basis, the Floquet state $|w_j(t)\rangle$ has the decomposition

$$|w_j(t)\rangle = \sum_{k\in\mathbb{Z}}\sum_{\sigma=z^\pm} u_{j\sigma k}|\sigma\rangle e^{-ik\omega_{\rm d}t}, \tag{D1}$$

which is the Fourier expansion of $|w_j(t)\rangle$ with $u_{j\sigma k}$ as Fourier coefficients. It is useful to define an inner product for elements of $\mathcal{F}$ via the time average of their product over one drive period. Based on this definition, the basis $\{|f_{\sigma,k}(t)\rangle\}$ is orthonormal, since

$$\frac{\omega_{\rm d}}{2\pi}\int_0^{2\pi/\omega_{\rm d}}\mathrm{d}t\,\langle f_{\sigma,k}(t)|f_{\sigma',k'}(t)\rangle = \delta_{\sigma\sigma'}\delta_{kk'}. \tag{D2}$$

The decomposition (D1) maps the periodic function $|w_j(t)\rangle\in\mathcal{F}$ to a vector $\vec{\mathbf{u}}_j\in\mathcal{V} = \mathbb{C}^2\otimes\mathbb{C}^\infty$. Here, the basis vectors $|f_{\sigma,k}(t)\rangle$ of $\mathcal{F}$ are mapped to the canonical unit vectors $(\vec{\mathbf{u}})_{\sigma',k'} = \delta_{\sigma\sigma'}\delta_{kk'}$ which we also denote by $|\sigma,k\rangle$. Following this basis change, the Floquet state Eq. (D1) is now represented as a vector in $\mathcal{V}$,

$$|\bar{w}_j\rangle = \sum_{\sigma=z^\pm}\sum_{k\in\mathbb{Z}} u_{j\sigma k}|\sigma,k\rangle. \tag{D3}$$

Applying the basis change to the Floquet equation, one finds that it converts to an ordinary eigenvalue problem. To carry out this step, we consider the two operators $H_{\rm q}(t)$ and $-i\partial/\partial t$ acting on $|w_j(t)\rangle$ on the left-hand side of Eq. (4). Both of them map basis functions $|f_{\sigma,k}(t)\rangle$ to other time-periodic functions in $\mathcal{F}$, and hence correspond to matrices acting on elements in $\mathcal{V}$. Specifically, we have

$$\begin{aligned}H_{\rm q}(t)|f_{\sigma,k}(t)\rangle &= \sum_{\sigma,\sigma'=z^\pm}\sum_{k'\in\mathbb{Z}} h_{\sigma'\sigma k'}|f_{\sigma',k+k'}(t)\rangle, \\ -i\frac{\partial}{\partial t}|f_{\sigma,k}(t)\rangle &= -k\omega_{\rm d}|f_{\sigma,k}(t)\rangle,\end{aligned} \tag{D4}$$

where

$$h_{\sigma'\sigma k'} = \frac{\omega_{\rm d}}{2\pi}\int_0^{2\pi/\omega_{\rm d}} {\rm d}t\, e^{ik'\omega_{\rm d}t}\langle\sigma'|H_{\rm q}(t)|\sigma\rangle.$$

Using Eq. (D4), we can easily express the matrices representing $H_{\rm q}(t)$ and $-i\partial/\partial t$ as

$$\begin{aligned}\bar{H}_{\rm q} &= \sum_{\sigma,\sigma'=z^\pm}\sum_{k,k'\in\mathbb{Z}} h_{\sigma'\sigma'k'}|\sigma',k+k'\rangle\langle\sigma,k|, \qquad \text{(D5)}\\ \bar{\Lambda} &= -\sum_{\sigma=z^\pm}\sum_{k\in\mathbb{Z}} k\omega_{\rm d}|\sigma,k\rangle\langle\sigma,k|.\end{aligned}$$

With this the Floquet equation takes on the form

$$\bar{H}|\bar{w}_j\rangle = \epsilon_j|\bar{w}_j\rangle, \qquad \text{(D6)}$$

where $\bar{H} = \bar{H}_{\rm q} + \bar{\Lambda}$.

Solving this eigenvalue equation yields an infinite number of eigenvectors and corresponding eigenvalues (quasi-energies). The structure of this equation is such that any given eigenpair $|\bar{w}_j\rangle$, ϵ_j generates an infinite set of solutions defined via

$$\begin{aligned}|\bar{w}_{j,n}\rangle &= \sum_{\sigma=z^\pm}\sum_{k\in\mathbb{Z}} u_{j\sigma,k}|\sigma,k-n\rangle,\\ \epsilon_{j,n} &= \epsilon_j + n\omega_{\rm d}\ (n\in\mathbb{Z}). \qquad \text{(D7)}\end{aligned}$$

Reverting back to the function space $\mathcal{F}$, the above states have the form $|w_{j,n}(t)\rangle = |w_j(t)\rangle\exp(-in\omega_{\rm d}t)$. Accordingly, at the level of the underlying Hilbert space of quantum states, only two of these states ($j = 0, 1$) are linearly independent.

In the following, we employ this Floquet framework to the specific Hamiltonian (1). For this analysis, it is useful to provide explicit expressions for the transformed $\bar{H}_{\rm q}$ from $H_{\rm q}(t)$. $H_{\rm q}(t)$ involves three distinct operations: $\hat{\sigma}_x$, $\hat{\sigma}_z$, and $\hat{\sigma}_z\cos\omega_{\rm d}t$ which are all valid linear operators on the function space $\mathcal{F}$. Applying again the basis transformation that led from Eq. (D4) to Eq. (D5), these operators are transformed to the following matrices in the $|\sigma,k\rangle$ basis:

$$\begin{aligned}\bar{\sigma}_x &= \sum_{k\in\mathbb{Z}}|z^+,k\rangle\langle z^-,k| + |z^-,k\rangle\langle z^+,k|,\\ \bar{\sigma}_z &= \sum_{k\in\mathbb{Z}}|z^+,k\rangle\langle z^+,k| - |z^-,k\rangle\langle z^-,k|, \qquad \text{(D8)}\\ \bar{\sigma}_{z,{\rm d}} &= \frac{1}{2}\sum_{k'=\pm1}\sum_{k\in\mathbb{Z}}|z^+,k+k'\rangle\langle z^+,k| - |z^-,k+k'\rangle\langle z^-,k|.\end{aligned}$$

The resulting $\bar{H}_{\rm q}$ can then be compactly written as

$$\bar{H}_{\rm q} = \frac{\Delta}{2}\bar{\sigma}_x + \left(A\bar{\sigma}_{z,{\rm d}} + \frac{B}{2}\bar{\sigma}_z\right). \qquad \text{(D9)}$$

1. Relating $\partial\epsilon_{01}/\partial B$ to $g_{k,\mu}$

Here, we establish the relation between the derivative $\partial\epsilon_{01}/\partial B \sim \partial\epsilon_{01}/\partial\phi_{\rm dc}$ and the coefficients $g_{k,\mu}$. We consider a small perturbation affecting the Floquet Hamiltonian (D9) of the type $\bar{H}_{\rm q} \to \bar{H}_{\rm q} + \delta B\,\bar{\sigma}_z/2$. The first-order correction to the quasi-energy difference ϵ_{01} is given by

$$\delta\epsilon_{01}^{(1)} = \frac{\delta B}{2}\left(\langle\bar{w}_1|\bar{\sigma}_z|\bar{w}_1\rangle - \langle\bar{w}_0|\bar{\sigma}_z|\bar{w}_0\rangle\right). \qquad \text{(D10)}$$

Making use of the definition of $\bar{\sigma}_z$ in Eq. (D8) and the inner product, we find

$$\langle\bar{w}_j|\bar{\sigma}_z|\bar{w}_{j'}\rangle = \frac{\omega_{\rm d}}{2\pi}\int_0^{2\pi/\omega_{\rm d}}{\rm d}t\,\langle w_j(t)|\hat{\sigma}_z|w_{j'}(t)\rangle, \qquad \text{(D11)}$$

and thus arrive at the identity

$$\delta\epsilon_{01}^{(1)} = \frac{\delta B}{2}\times\frac{\omega_{\rm d}}{2\pi}\int_0^{2\pi/\omega_{\rm d}}{\rm d}t\ {\rm Tr}_{\rm q}[\hat{\sigma}_z\hat{c}_z(t)] = \delta B\, g_{0,\phi}, \qquad \text{(D12)}$$

where the last step uses the definition of $g_{0,\phi}$ from Eq. (B4). We thus conclude that $\partial\epsilon_{01}/\partial B = g_{0,\phi}$.

2. Avoided crossings in the strong-drive limit

In this and the following subsections, we employ perturbation theory to estimate the gap sizes of avoided crossings, in the strong-drive ($A \gtrsim \Omega_{ge}$) and weak-drive ($A \ll \Omega_{ge}$) limit. In the strong-drive limit, we treat the first term $\bar{V} = \Delta\bar{\sigma}_x/2$ in (D9) perturbatively while $\bar{H}_0 = \bar{H} - \bar{V}$ acts as the unperturbed Hamiltonian. The exact eigenstates and eigenvalues of $\bar{H}_0$ are [45, 46]

$$\begin{aligned}\left|\bar{w}^{(0)}_{\pm,n}\right\rangle &= \sum_{k\in\mathbb{Z}} J_k\left(\mp\frac{A}{\omega_{\rm d}}\right)|z^\pm,k-n\rangle, \qquad \text{(D13)}\\ \epsilon_{\pm,n} &= \pm B/2 + n\omega_{\rm d}.\end{aligned}$$

Here, we have chosen to adjuster notation according to $j = 0,1 \to \pm$ which helps keep expressions in the following more compact, but should not be confused with the notation $z^\pm$.

Whenever the drive frequency matches $\omega_{\rm d} = B/m$ ($m \in \mathbb{N}$), one finds that the unperturbed quasi-energies $\epsilon_{+,n}$ become $\epsilon_{-,n+m}$ degenerate. This degeneracy is lifted when including corrections of first order in Δ. Perturbation theory yields

$$\Delta_m^{(1)} = 2\left|\left\langle\bar{w}^{(0)}_{+,0}\middle|\bar{V}\middle|\bar{w}^{(0)}_{-,m}\right\rangle\right| = \Delta\left|\left\langle\bar{w}^{(0)}_{+,0}\middle|\bar{\sigma}_x\middle|\bar{w}^{(0)}_{-,m}\right\rangle\right|.$$

To proceed, we convert the Floquet states back into the time domain via

$$\left|w^{(0)}_{\pm,n}(t)\right\rangle = \exp\left(\mp i\frac{A}{\omega_{\rm d}}\sin\omega_{\rm d}t + in\omega_{\rm d}t\right)|z^\pm\rangle. \qquad \text{(D14)}$$

(Note that Eqs. (D13) and (D14) are related through the Jacobi-Anger expansion.) This enables the evaluation of the leading-order gap size:

$$\begin{aligned}\Delta_m^{(1)} &= \Delta\left|\frac{\omega_{\rm d}}{2\pi}\int_0^{2\pi/\omega_{\rm d}}{\rm d}t\,\left\langle w^{(0)}_{+,0}(t)\middle|\hat{\sigma}_x\middle|w^{(0)}_{-,m}(t)\right\rangle\right|\\ &= \Delta\left|J_m\left(\frac{2A}{\omega_{\rm d}}\right)\right|. \qquad \text{(D15)}\end{aligned}$$

3. Avoided crossings in the weak-drive limit

In the weak-drive limit ($A \ll \Omega_{ge}$), we instead treat the drive-related term $\bar{V} = A\,\bar{\sigma}_{z,\mathrm{d}}$ perturbatively. The unperturbed eigenvalues and eigenstates of $\bar{H}_0 = \bar{H} - \bar{V}$ are given by

$$\left|\bar{w}^{(0)}_{\pm,n}\right\rangle = \cos\frac{\theta}{2}\,|z^{\pm}, -n\rangle \pm \sin\frac{\theta}{2}\,|z^{\mp}, -n\rangle, \tag{D16}$$

$$\epsilon_{\pm,n} = \pm\Omega_{ge}/2 + n\omega_{\mathrm{d}}. \tag{D17}$$

These are closely related to the eigenstates and eigenvalues of the undriven qubit. Here, we employ the definitions $\theta = \tan^{-1}(\Delta/B)$, and $\Omega_{ge} = \sqrt{\Delta^2 + B^2}$.

Whenever the drive frequency obeys $\omega_{\mathrm{d}} = \Omega_{ge}/m$ ($m \in \mathbb{N}$), the quasi-energies $\epsilon_{+,n} = \epsilon_{-,n+m}$ become degenerate. Again, this degeneracy is lifted by the perturbation $\bar{V}$. For $m = 1$, the calculation resembles the one for the strong-drive limit and results in a leading-order gap size of

$$\Delta^{(1)}_{m=1} = 2\left|\left\langle \bar{w}^{(0)}_{+,0}\middle|\bar{V}\middle|\bar{w}^{(0)}_{-,1}\right\rangle\right| = A|\sin\theta|. \tag{D18}$$

The calculation of the gap sizes for $m > 1$ requires higher-order degenerate perturbation theory, which we perform using Brillouin-Wigner expansion. This approach converts Eq. (D6) into a reduced equation that only involves the degenerate eigenvector pair $|\bar{w}^{(0)}_{+,0}\rangle$ and $|\bar{w}^{(0)}_{-,m}\rangle$.

To facilitate the derivation of the reduced equation, we define the projection operators

$$\bar{P} = \left|\bar{w}^{(0)}_{+,0}\right\rangle\left\langle\bar{w}^{(0)}_{+,0}\right| + \left|\bar{w}^{(0)}_{-,m}\right\rangle\left\langle\bar{w}^{(0)}_{-,m}\right|$$

and $\bar{Q} = \bar{\mathbb{1}} - \bar{P}$, which project vectors in $\mathcal{V}$ onto the degenerate subspace, and onto the subspace orthogonal to it, respectively. Here, $\bar{\mathbb{1}}$ is the identity operator on $\mathcal{V}$. According to Brillouin-Wigner theory, the two exact eigenvectors $|\bar{w}_j\rangle$ with quasi-energy ϵ_j obey the equation

$$\bar{H}_{\mathrm{deg}}|\bar{w}_j\rangle = \epsilon_j|\bar{w}_j\rangle, \tag{D19}$$

where

$$\bar{H}_{\mathrm{deg}} = \bar{P}(\bar{V} + \bar{V}\bar{T}\bar{V} + \bar{V}\bar{T}\bar{V}\bar{T}\bar{V} + \cdots)\bar{P}, \tag{D20}$$

and

$$\bar{T} = \frac{\bar{Q}}{\epsilon_j - \bar{H}_0}. \tag{D21}$$

Note that despite its appearance, Eq. (D19) is not an ordinary eigenvalue problem, since both sides contain the eigenvalue ϵ_j. It is possible to find a solution for the eigenvalues iteratively. To avoid excessive notation, we focus on the $j = 0$ eigenvalue and omit unnecessary subscripts in the following. In the first iteration, we insert the unperturbed quasi-energy $\epsilon^{(0)} = \epsilon_{+,0}$ into the left-hand side of Eq. (D19), and solve for $\epsilon^{(1)}$ on the right-hand side. Using the new quasi-energy approximation, we then repeat these steps to include higher-order corrections. With this procedure, we find that, to leading order in A, the gap size is given by

$$\Delta_m \approx |\sin\theta\cos^{m-1}\theta|\frac{A^m}{(m-1)!\,\omega_{\mathrm{d}}^{m-1}}. \tag{D22}$$

4. Gap size and the width of T_ϕ peaks surrounding sweet-spot manifolds

In this subsection, we establish the relation between the gap size Δ_m and the width of the T_ϕ peaks along the drive-frequency axis surrounding sweet-spot manifolds. We derive this relation only for the strong-drive limit; the derivation for the weak-drive limit is analogous.

Generically, the pure-dephasing rate of a Floquet qubit is likely to be dominated by the $1/f$ noise contributions away from sweet spots. In our case, that noise correspond to flux noise which limits the system, whenever the derivative of the quasi-energy difference with respect to flux is nonzero, $\partial\epsilon_{01}/\partial B \neq 0$. Under these conditions, Eq. (8) implies that T_ϕ is inversely proportional to $|\partial\epsilon_{01}/\partial B|$. Therefore, to find the drive-frequency width of the T_ϕ peaks, it is useful to first explore how $|\partial\epsilon_{01}/\partial B|$ depends on ω_{d}.

For a dynamical sweet spot in the strong-drive limit, $A_0 \gg \Omega_{ge}$, the drive parameters satisfy $\omega_{\mathrm{d},m} = B_0/m$. At the sweet spot, the quasi-energy derivative vanishes, $\partial\epsilon_{01}/\partial B = 0$. Let us consider values B and ω_{d} in the vicinity of the sweet-spot point given by B_0 and $\omega_{\mathrm{d},m}$. Using Eq. (D13), we see that the Hamiltonian in the relevant subspace is

$$\begin{aligned}\bar{H} &= \bar{H}_0 + \bar{V} \\ &= \epsilon_{+,0}|\bar{w}^{(0)}_{+,0}\rangle\langle\bar{w}^{(0)}_{+,0}| + \epsilon_{-,m}|\bar{w}^{(0)}_{-,m}\rangle\langle\bar{w}^{(0)}_{-,m}| + \Delta\bar{\sigma}_x/2,\end{aligned} \tag{D23}$$

which results in the quasi-energy difference

$$\epsilon_{01} \approx \sqrt{\Delta_m^2 + (B - m\omega_{\mathrm{d}})^2}. \tag{D24}$$

The derivative of ϵ_{01} with respect to B is thus

$$\frac{\partial\epsilon_{01}}{\partial B} \approx \frac{B - m\omega_{\mathrm{d}}}{\epsilon_{01}}. \tag{D25}$$

Since we are interested in the width of the sweet manifold along the ω_{d}-axis, we set $B = B_0$, and consider variations of ω_{d} around $\omega_{\mathrm{d},m}$. As a function of ω_{d}, the derivative $|\partial\epsilon_{01}/\partial B|$ takes on its minimum value of zero at $\omega_{\mathrm{d}} = \omega_{\mathrm{d},m}$. Away from this sweet spot, $|\partial\epsilon_{01}/\partial B|$ has an upper bound of 1, which is reached asymptotically in the limit $m|\omega_{\mathrm{d}} - \omega_{\mathrm{d},m}| \gg \Delta_m$. Based on this, we can use the full width at half minimum (FWHm) of $|\partial\epsilon_{01}/\partial B|$ as an estimate of the peak width of T_ϕ. The condition $|\partial\epsilon_{01}/\partial B| = 1/2$ for reaching the half-minimum value, results in the equation

$$\frac{m|\omega_{\mathrm{d}} - \omega_{\mathrm{d},m}|}{\sqrt{\Delta_m^2 + m^2(\omega_{\mathrm{d}} - \omega_{\mathrm{d},m})^2}} = \frac{1}{2}. \tag{D26}$$

The corresponding two solutions $\omega_{\mathrm{d}}^{(1,2)}$ yield the FWHm $|\omega_{\mathrm{d}}^{(2)} - \omega_{\mathrm{d}}^{(1)}|$. Due the dependence of Δ_m on ω_{d} involving a Bessel function [Eq. (D15)], the above equation (D26) is transcendental. We can obtain analytical approximations as follows. We rewrite Eq. (D26) in the form $\sqrt{3}m|\omega_{\mathrm{d}} - \omega_{\mathrm{d},m}| = \Delta_m$, and expanding the latter in ω_{d} around $\omega_{\mathrm{d},m}$. The result of this is another transcendental equation, in which the problematic Bessel function term can, however, be neglected

if $\partial\Delta_m/\partial\omega_\mathrm{d} \ll \sqrt{3}m$ holds. We have verified the validity of this inequality for our parameters numerically, and this way finally obtain the approximate FWHm

$$\Delta\omega_\mathrm{FWHm} = 2\Delta_{m,0}/\sqrt{3}m, \tag{D27}$$

where $\Delta_{m,0} = \Delta|J_m(2A_0/\omega_{\mathrm{d},m})|$.

[1] C. H. van der Wal, A. C. J. ter Haar, F. K. Wilhelm, R. N. Schouten, C. J. P. M. Harmans, T. P. Orlando, S. Lloyd, and J. E. Mooij, *Quantum Superposition of Macroscopic Persistent-Current States*, Science **290**, 773 (2000).

[2] Y. Nakamura, Y. A. Pashkin, T. Yamamoto, and J. S. Tsai, *Charge Echo in a Cooper-Pair Box*, Phys. Rev. Lett. **88**, 047901 (2002).

[3] F. Yoshihara, K. Harrabi, A. O. Niskanen, Y. Nakamura, and J. S. Tsai, *Decoherence of Flux Qubits due to* $1/f$ *Flux Noise*, Phys. Rev. Lett. **97**, 167001 (2006).

[4] S. M. Anton, C. Müller, J. S. Birenbaum, S. R. O'Kelley, A. D. Fefferman, D. S. Golubev, G. C. Hilton, H.-M. Cho, K. D. Irwin, F. C. Wellstood, G. Schön, A. Shnirman, and J. Clarke, *Pure dephasing in flux qubits due to flux noise with spectral density scaling as* $1/f^\alpha$, Phys. Rev. B **85**, 224505 (2012).

[5] G. Ithier, E. Collin, P. Joyez, P. J. Meeson, D. Vion, D. Esteve, F. Chiarello, A. Shnirman, Y. Makhlin, J. Schriefl, and G. Schön, *Decoherence in a superconducting quantum bit circuit*, Phys. Rev. B **72**, 134519 (2005).

[6] J. Koch, T. M. Yu, J. Gambetta, A. A. Houck, D. I. Schuster, J. Majer, A. Blais, M. H. Devoret, S. M. Girvin, and R. J. Schoelkopf, *Charge-insensitive qubit design derived from the Cooper pair box*, Phys. Rev. A **76**, 042319 (2007).

[7] L. B. Nguyen, Y.-H. Lin, A. Somoroff, R. Mencia, N. Grabon, and V. E. Manucharyan, *High-Coherence Fluxonium Qubit*, Phys. Rev. X **9**, 041041 (2019).

[8] H. Zhang, S. Chakram, T. Roy, N. Earnest, Y. Lu, Z. Huang, D. Weiss, J. Koch, and D. I. Schuster, *Universal fast flux control of a coherent, low-frequency qubit*, arXiv:2002.10653.

[9] M. D. Hutchings, J. B. Hertzberg, Y. Liu, N. T. Bronn, G. A. Keefe, M. Brink, J. M. Chow, and B. L. T. Plourde, *Tunable Superconducting Qubits with Flux-Independent Coherence*, Phys. Rev. Applied **8**, 044003 (2017).

[10] R. Barends, J. Kelly, A. Megrant, D. Sank, E. Jeffrey, Y. Chen, Y. Yin, B. Chiaro, J. Mutus, C. Neill, P. O'Malley, P. Roushan, J. Wenner, T. C. White, A. N. Cleland, and J. M. Martinis, *Coherent Josephson Qubit Suitable for Scalable Quantum Integrated Circuits*, Phys. Rev. Lett. **111**, 080502 (2013).

[11] N. Earnest, S. Chakram, Y. Lu, N. Irons, R. K. Naik, N. Leung, L. Ocola, D. A. Czaplewski, B. Baker, J. Lawrence, J. Koch, and D. I. Schuster, *Realization of a* Λ *System with Metastable States of a Capacitively Shunted Fluxonium*, Phys. Rev. Lett. **120**, 150504 (2018).

[12] Y.-H. Lin, L. B. Nguyen, N. Grabon, J. San Miguel, N. Pankratova, and V. E. Manucharyan, *Demonstration of Protection of a Superconducting Qubit from Energy Decay*, Phys. Rev. Lett. **120**, 150503 (2018).

[13] T. M. Hazard, A. Gyenis, A. Di Paolo, A. T. Asfaw, S. A. Lyon, A. Blais, and A. A. Houck, *Nanowire Superinductance Fluxonium Qubit*, Phys. Rev. Lett. **122**, 010504 (2019).

[14] J. M. Martinis, S. Nam, J. Aumentado, K. M. Lang, and C. Urbina, *Decoherence of a superconducting qubit due to bias noise*, Phys. Rev. B **67**, 094510 (2003).

[15] C. M. Quintana, Y. Chen, D. Sank, A. G. Petukhov, T. C. White, D. Kafri, B. Chiaro, A. Megrant, R. Barends, B. Campbell, Z. Chen, A. Dunsworth, A. G. Fowler, R. Graff, E. Jeffrey, J. Kelly, E. Lucero, J. Y. Mutus, M. Neeley, C. Neill, P. J. J. O'Malley, P. Roushan, A. Shabani, V. N. Smelyanskiy, A. Vainsencher, J. Wenner, H. Neven, and J. M. Martinis, *Observation of Classical-Quantum Crossover of* $1/f$ *Flux Noise and Its Paramagnetic Temperature Dependence*, Phys. Rev. Lett. **118**, 057702 (2017).

[16] A. Kou, W. C. Smith, U. Vool, R. T. Brierley, H. Meier, L. Frunzio, S. M. Girvin, L. I. Glazman, and M. H. Devoret, *Fluxonium-Based Artificial Molecule with a Tunable Magnetic Moment*, Phys. Rev. X **7**, 031037 (2017).

[17] J. Bylander, S. Gustavsson, F. Yan, F. Yoshihara, K. Harrabi, G. Fitch, D. G. Cory, Y. Nakamura, J.-S. Tsai, and W. D. Oliver, *Noise spectroscopy through dynamical decoupling with a superconducting flux qubit*, Nat. Phys. **7**, 565 (2011).

[18] J. R. Petta, A. C. Johnson, J. M. Taylor, E. A. Laird, A. Yacoby, M. D. Lukin, C. M. Marcus, M. P. Hanson, and A. C. Gossard, *Coherent Manipulation of Coupled Electron Spins in Semiconductor Quantum Dots*, Science **309**, 2180 (2005).

[19] F. H. L. Koppens, K. C. Nowack, and L. M. K. Vandersypen, *Spin Echo of a Single Electron Spin in a Quantum Dot*, Phys. Rev. Lett. **100**, 236802 (2008).

[20] H. Bluhm, S. Foletti, I. Neder, M. Rudner, D. Mahalu, V. Umansky, and A. Yacoby, *Dephasing time of GaAs electron-spin qubits coupled to a nuclear bath exceeding 200* μ*s*, Nat. Phys. **2**, 109 (2011).

[21] A. Safavi-Naini, P. Rabl, P. F. Weck, and H. R. Sadeghpour, *Microscopic model of electric-field-noise heating in ion traps*, Phys. Rev. A **84**, 023412 (2011).

[22] N. Daniilidis, S. Narayanan, S. A. Mller, R. Clark, T. E. Lee, P. J. Leek, A. Wallraff, S. Schulz, F. Schmidt-Kaler, and H. Hffner, *Fabrication and heating rate study of microscopic surface electrode ion traps*, New J. Phys. **13**, 013032 (2011).

[23] M. Brownnutt, M. Kumph, P. Rabl, and R. Blatt, *Ion-trap measurements of electric-field noise near surfaces*, Rev. Mod. Phys. **87**, 1419 (2015).

[24] K. Khodjasteh and D. A. Lidar, *Fault-Tolerant Quantum Dynamical Decoupling*, Phys. Rev. Lett. **95**, 180501 (2005).

[25] B. Pokharel, N. Anand, B. Fortman, and D. A. Lidar, *Demonstration of Fidelity Improvement Using Dynamical Decoupling with Superconducting Qubits*, Phys. Rev. Lett. **121**, 220502 (2018).

[26] L. Cywiński, R. M. Lutchyn, C. P. Nave, and S. Das Sarma, *How to enhance dephasing time in superconducting qubits*, Phys. Rev. B **77**, 174509 (2008).

[27] L. Viola, E. Knill, and S. Lloyd, *Dynamical Decoupling of Open Quantum Systems*, Phys. Rev. Lett. **82**, 2417 (1999).

[28] G. S. Uhrig, *Keeping a Quantum Bit Alive by Optimized* π*-Pulse Sequences*, Phys. Rev. Lett. **98**, 100504 (2007).

[29] E. L. Hahn, *Spin echoes*, Phys. Rev. **80**, 580 (1950).

[30] H. Y. Carr and E. M. Purcell, *Effects of Diffusion on Free Precession in Nuclear Magnetic Resonance Experiments*, Phys. Rev. **94**, 630 (1954).

[31] S. Meiboom and D. Gill, *Modified SpinEcho Method for Measuring Nuclear Relaxation Times*, Rev. Sci. Instrum. **29**, 688 (1958).

[32] N. Didier, E. A. Sete, J. Combes, and M. P. da Silva, *ac Flux Sweet Spots in Parametrically Modulated Superconducting Qubits*, Phys. Rev. Applied **12**, 054015 (2019).

[33] S. S. Hong, A. T. Papageorge, P. Sivarajah, G. Crossman, N. Didier, A. M. Polloreno, E. A. Sete, S. W. Turkowski, M. P. da Silva, and B. R. Johnson, *Demonstration of a parametrically activated entangling gate protected from flux noise*, Phys. Rev. A **101**, 012302 (2020).

[34] N. Didier, *Flux control of superconducting qubits at dynamical sweet spots*, arXiv:1912.09416.

[35] L. Viola and E. Knill, *Robust Dynamical Decoupling of Quantum Systems with Bounded Controls*, Phys. Rev. Lett. **90**, 037901 (2003).

[36] Q. Guo, S.-B. Zheng, J. Wang, C. Song, P. Zhang, K. Li, W. Liu, H. Deng, K. Huang, D. Zheng, X. Zhu, H. Wang, C.-Y. Lu, and J.-W. Pan, *Dephasing-Insensitive Quantum Information Storage and Processing with Superconducting Qubits*, Phys. Rev. Lett. **121**, 130501 (2018).

[37] F. Yan, S. Gustavsson, J. Bylander, X. Jin, F. Yoshihara, D. G. Cory, Y. Nakamura, T. P. Orlando, and W. D. Oliver, *Rotating-frame relaxation as a noise spectrum analyser of a superconducting qubit undergoing driven evolution*, Nature Communications **4**, 10.1038/ncomms3337 (2013).

[38] J. Jing, P. Huang, and X. Hu, *Decoherence of an electrically driven spin qubit*, Phys. Rev. A **90**, 022118 (2014).

[39] V. E. Manucharyan, J. Koch, L. I. Glazman, and M. H. Devoret, *Fluxonium: Single Cooper-Pair Circuit Free of Charge Offsets*, Science **326**, 113 (2009).

[40] At low frequencies $\omega \ll k_B T$, the asymmetry in the spectrum is negligible and a symmetric 1/f noise spectrum may be used.

[41] P. Groszkowski, A. D. Paolo, A. L. Grimsmo, A. Blais, D. I. Schuster, A. A. Houck, and J. Koch, *Coherence properties of the 0-π qubit*, New J. Phys. **20**, 043053 (2018).

[42] W. Smith, A. Kou, X. Xiao, U. Vool, and M. Devoret, *Superconducting circuit protected by two-Cooper-pair tunneling*, npj Quantum Information **6**, 8 (2020).

[43] S. Kohler, T. Dittrich, and P. Hänggi, *Floquet-Markovian description of the parametrically driven, dissipative harmonic quantum oscillator*, Phys. Rev. E **55**, 300 (1997).

[44] H. Breuer and F. Petruccione, *The Theory of Open Quantum Systems* (Oxford University Press, New York, 2007).

[45] S.-K. Son, S. Han, and S.-I. Chu, *Floquet formulation for the investigation of multiphoton quantum interference in a superconducting qubit driven by a strong ac field*, Phys. Rev. A **79**, 032301 (2009).

[46] C. Deng, J.-L. Orgiazzi, F. Shen, S. Ashhab, and A. Lupascu, *Observation of Floquet States in a Strongly Driven Artificial Atom*, Phys. Rev. Lett. **115**, 133601 (2015).

[47] J. Hausinger and M. Grifoni, *Dissipative two-level system under strong ac driving: A combination of Floquet and Van Vleck perturbation theory*, Phys. Rev. A **81**, 022117 (2010).

[48] Due to the non-exponential decay for $1/f$ noise, the relationship between rate and filter function has to be modified (see Appendix C).

[49] S. Ashhab, J. R. Johansson, A. M. Zagoskin, and F. Nori, *Two-level systems driven by large-amplitude fields*, Phys. Rev. A **75**, 063414 (2007).

[50] P. Mundada, A. Gyenis, Z. Huang, J. Koch, and A. Houck, manuscript in preparation.

[51] S. Guérin, *Complete dissociation by chirped laser pulses designed by adiabatic Floquet analysis*, Phys. Rev. A **56**, 1458 (1997).

[52] X. You, J. A. Sauls, and J. Koch, *Circuit quantization in the presence of time-dependent external flux*, Phys. Rev. B **99**, 174512 (2019).